PNAS RESEARCH ARTICLE | CHEMISTRY

Triggered lattice-oxygen oxidation with active-site generation and self-termination of surface reconstruction during water oxidation

Yicheng Wei[a,1], Yang Hu[a,1], Pengfei Da[a], Zheng Weng[a], Pinxian Xi[a,b,2], and Chun-Hua Yan[a,c]

Edited by Alexis Bell, University of California, Berkeley, CA; received July 18, 2023; accepted September 22, 2023

To master the activation law and mechanism of surface lattice oxygen for the oxygen evolution reaction (OER) is critical for the development of efficient water electrolysis. Herein, we propose a strategy for triggering lattice-oxygen oxidation and enabling non-concerted proton–electron transfers during OER conditions by substituting Al in $La_{0.3}Sr_{0.7}CoO_{3-\delta}$. According to our experimental data and density functional theory calculations, the substitution of Al can have a dual effect of promoting surface reconstruction into active Co oxyhydroxides and activating deprotonation on the reconstructed oxyhydroxide, inducing negatively charged oxygen as an active site. This leads to a significant improvement in the OER activity. Additionally, Al dopants facilitate the preoxidation of active cobalt metal, which introduces great structural flexibility due to elevated O 2*p* levels. As OER progresses, the accumulation of oxygen vacancies and lattice-oxygen oxidation on the catalyst surface leads to the termination of Al^{3+} leaching, thereby preventing further reconstruction. We have demonstrated a promising approach to achieving tunable electrochemical reconstruction by optimizing the electronic structure and gained a fundamental understanding of the activation mechanism of surface oxygen sites.

perovskite oxide | lattice-oxygen oxidation | surface reconstruction | self-termination | oxygen evolution reaction

With the rapid development of the research on the mechanism of electrocatalytic oxygen evolution reaction (OER) in the catalytic process, the current understanding of the OER mechanism of metal oxides is not limited to the study of the redox chemistry of the metal cation surfaces anymore, involving four coordinated proton–electron transfer steps at the surface metal ion center (1–3). Involving the redox and the migration of surface lattice oxygen has been proven to be very important in various applications such as catalyzing OER in photo-electrochemical water splitting, regenerative fuel cells, rechargeable metal–air batteries, and energy storage in lithium-ion battery materials (4–10). Therefore, understanding the anionic redox chemistry of oxygen in metal oxides, on the surface and in the bulk, is crucial for the development of efficient energy storage technologies that require materials capable of catalyzing OER.

Recent reports have shown that highly active oxides exhibit pH-dependent OER activity on the RHE (reversible hydrogen electrode) scale, indicating that non-concerted proton–electron transfers are involved in catalyzing the OER catalysts (11–13). This oxidation reaction occurs on the lattice oxygen of oxides, known as the lattice-oxygen oxidation mechanism (LOM), and is determined by the inherent metal–oxygen covalent property of the catalyst (14). During the LOM process, the catalysts often undergo surface reconstruction due to redox reactions and the migration of lattice oxygen, which can significantly reduce their stability (11). The perovskite oxides have a high structural tolerance, which allows for the adjustment and regulation of their metal 3*d* and O 2*p* band structures over a wide range (15). Therefore, activating the anionic redox chemistry of oxygen in perovskites is a relatively reliable approach. Previous studies have shown that enhancing the O 2*p*–band centre (defined relative to the Fermi level), while decreasing metal–oxygen hybridization, can lead to improved OER activity. This suggests that the bulk electronic structure plays a crucial role in catalysing OER kinetics (16–19). However, the proper method for promoting surface reconstruction to achieve this effect is still unclear. Additionally, it is important to control surface reconstruction to prevent any impact on the volume of oxide catalysts used as templates for creating highly reactive surfaces. Thus, it is highly desirable to develop strategies for activating and terminating the surface reconstruction.

Herein, we constructed different perovskites by finely regulating two different environments of Al species in each $La_{0.3}Sr_{0.7}Co_{1-x}Al_xO_{3-}\delta$ (LSCAO) sample. The substitution of

Significance

This work has resolved several existing problems in the field of materials science: a) Why Al substitution the $La_{0.3}Sr_{0.7}CoO_{3-\delta}$ enable non-concerted proton-electron transfers during oxygen evolution reaction conditions, b) why Al dopants facilitate the preoxidation of active cobalt metal and Al^{3+} leaches at the beginning of reconstruction and further terminates the surface reconstruction. We directly probe the environments of Al species at a local scale by the ^{27}Al MAS NMR method with atomic-level resolution. Through finely controlled synthesis, we found two types of aluminum environments including AlO_6 octahedra and AlO_4 tetrahedra. Based on our density functional theory calculations, Al dopants facilitate the preoxidation of active cobalt metal, which also introduces great structural flexibility due to elevated O 2*p* levels.

Author contributions: P.X. and C.-H.Y. designed research; Y.W., Y.H., P.D., and Z.W. performed research; Y.W. and P.X. analyzed data; and Y.W. and P.X. wrote the paper.

The authors declare no competing interest.

This article is a PNAS Direct Submission.

[1]Y.W. and Y.H. contributed equally to this work.

[2]To whom correspondence may be addressed. Email: xipx@lzu.edu.cn.

This article contains supporting information online at https://www.pnas.org/lookup/suppl/doi:10.1073/pnas.2312224120/-/DCSupplemental.

Published December 5, 2023.

Al for Co in $La_{0.3}Sr_{0.7}CoO_{3-}\delta$ (LSCO) was found to promote surface remodeling by activating preoxidation of Co and optimizing the O 2*p*–band centre, leading to increased structural flexibility. Through a combination of experimental and theoretical approaches, it was demonstrated that this substitution can activate the oxidation of lattice oxygen in highly covalent metal oxides by non-catalytic active Al^{3+} substituting Co_{Oh}^{3+} in LSCO, triggering non-concerted proton–electron transfer and enhancing OER activity. Accurate electrochemical mass spectrometry measurements of ^{18}O-labelled perovskites have been implemented to directly quantify the oxidation of lattice oxygen during the OER. The results reveal that this process is more prevalent in less covalent oxides, such as LSCAOs oxide with different environments of Al species, compared to highly covalent LSCO. Less covalent oxides exhibit pH-dependent OER activities (on the RHE scale), whereas LSCO shows the pH-independent OER activity, which is expected from the conventional OER mechanism. Therefore, properly regulating the covalence of metal–oxygen bonds is crucial to initiate lattice-oxygen oxidation and allow non-concerted proton–electron transfers during OER.

Results

Crystal Structure Characterization. To study the activity of lattice-oxygen oxidation in perovskite LSCAOs under alkaline OER conditions, catalytically inactive Al^{3+} with p^6 electronic structure was used to substitute Co^{3+} in corresponding octahedral geometric configurations (Fig. 1*A*). By regulating the atomic ratio between Co and Al (*SI Appendix*, Fig. S1 and Table S1), we obtained the stoichiometric angles of LSCAO oxides using a sol–gel method (the Al substitution amount, $x \approx 0$ to 0.25). According to powder X-ray diffraction (XRD), the diffraction peaks of the as-synthesized LSCAO match with that of the standard cubic perovskite oxide (JCPDS: 48-0137, Fig. 1*B*). Such a peak shift could be ascribed to changes in lattice parameters induced by the different ionic radii of the Co and Al cations and suggests a solid solution property. Furthermore, the diffraction peaks for Al-doped samples are also found narrower and at different 2θ positions than those of undoped LSCO, as shown by the shifts of larger zoom of the (110) diffraction peak and shift to lower angles with increasing Al substitution amount; it suggests an expansion of the crystal lattice. This confirms the substitution of Co^{3+} with Al^{3+} in the LSCAOs sample which leads to an increase of the ahex one (20). This apparent contradiction can be attributed to a phenomenon called lattice strain caused by changes in local bonds. The scanning electron microscope images (*SI Appendix*, Fig. S2) and corresponding energy-dispersive X-ray spectroscopy (EDS) of the as-synthesized LSCAOs are in the form of nanoparticles (*SI Appendix*, Fig. S3), but their sizes are inevitably different. From the Brunauer–Emmett–Teller surface area (*SI Appendix*, Fig. S4), the as-synthesized oxide powders with different Al contents possess a specific surface area of 4 to 14 $m^2 g^{-1}$. The atomic resolution probe aberration-corrected high-angle annular dark-field scanning transmission electron microscopy (HAADF-STEM) and corresponding EDS elemental mapping of individual LSCO indicate the atom arrangement image and the uniform distribution of La, Sr, and Co atoms without phase segregation separation (*SI Appendix*, Fig. S5). The positive shifted Co $L_{2,3}$-edge in the atomic-column resolution electron energy loss spectrum (EELS) also supports an increased oxidation state of Co ions along with the Al substitution amount (Fig. 1*C* and *SI Appendix*, Fig. S6). To further explore the fine structure and the atomic-scale cation distributions of individual LSCAO (x = 0.20, sample was herby named LSCAO-0.2), HAADF-STEM images along [001] and [111] were directly taken to provide the atom arrangement images (Fig. 1*D* and *SI Appendix*, Fig. S7). The theoretical simulated STEM image confirms that the brightness of La–Sr columns at the cuboctahedra sites is more than that of Co–Al columns at the octahedral sites (the *Inset* of Fig. 1*D*). The schematic oriented crystal unit-cell model and atomic-resolution EDS elemental mappings of LSCAO-0.2 in Fig. 1*E* further illustrate that La/Sr are located at the A position of cuboctahedra sites in the crystal structure of

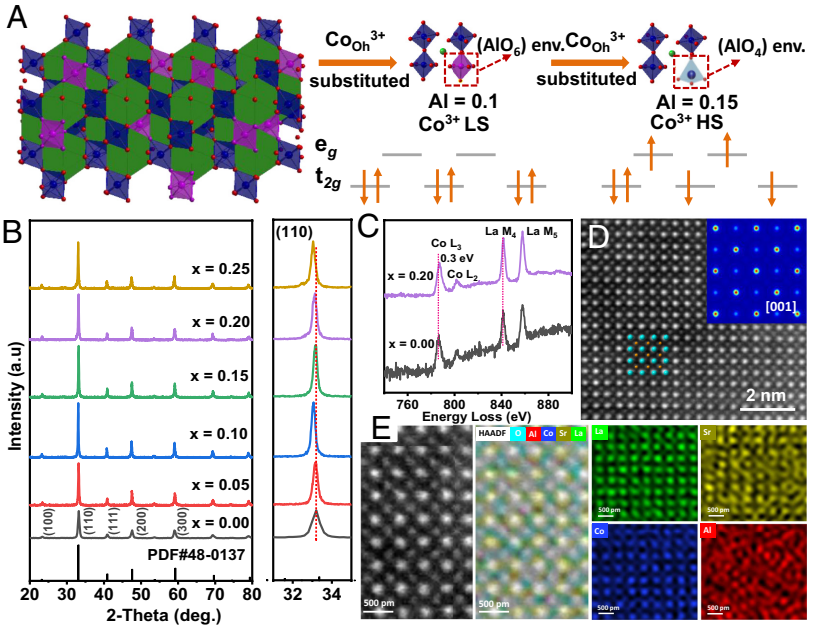

Fig. 1. Structural characterizations of as-prepared LSCAOs catalysts. (*A*) Schematic illustration of perovskite structures of LSCO, LSCAO-0.1, and LSCAO-0.15. (*B*) The XRD patterns for series of LSCAOs. (*C*) Co L-edge EELS spectra of LSCAOs with different Al substitution. (*D*) Atomic-resolution HAADF-STEM image of the partially inverse perovskite LSCAO-0.2 structure observed along [001] orientation. (*Inset*) Theoretical STEM images simulated by the Quantitative TEM/STEM Simulations Package (QSTEM) software projected along [001] orientation. (*E*) EDS atomic elemental mappings of the as-synthesized LSCAO-0.2.

ABO_3 perovskite oxide. However, it is also obvious that the Al points cannot overlap with the Co sites, where some Al sites show very evident deviations. The result shows that Co and Al are in different coordination environments at the B position of the crystal structure, which is consistent with XRD results.

In order to directly probe the environments of Al species in the LSCAOs product at a local scale, the ^{27}Al MAS NMR has been performed as a sophisticated method with atomic-level resolution (21–23). Consistent with the ^{27}Al shifts reported previously for aluminum oxides, typical AlO_6 octahedra (15 to 25 ppm) and AlO_4 tetrahedra (65 to 85 ppm) aluminum environments have been observed for Al-doped LSCAOs. It is apparent that when x = 0.1, the corresponding coordination environment of Al is different from the samples with x = 0.15 to 0.25, which is an evident switch between AlO_6 and AlO_4. This phenomenon should indicate a turning point for the Al environments. When the Al content increased to 0.15, the very broad and highly shifted ^{27}Al resonance (AlO_4 tetrahedra) can also be observed (Fig. 2*A*), which agrees with EDS elemental mappings results. The shift is governed for these systems due to *d*-orbital spin density transfer from paramagnetic transition metals via empty oxygen *p*-orbitals to nuclei under observation and is called the Fermi contact shift (24, 25). In addition to the complex behavior of Al-containing components throughout the oxides, Al substitution in LSCAOs also alters the local atomic structure of Co. As observed with the Fourier transform infrared spectroscopy of LSCAOs (*SI Appendix*, Fig. S8), the characteristic peaks for Co–O and O–Co–O vibrations move toward the lower wavenumber direction as the increase of Al amount from 0 to 0.25. It can be inferred that the vibration energy decreases. This is owing to that lattice distortion is induced by the coexistence of Co and Al which may lead to higher B–O stretching vibration and O–B–O bending vibration energy (26, 27). Moreover, the ultraviolet photo-electron spectroscopy (*SI Appendix*, Fig. S9) also has consistently shown that the successful incorporation of Al atoms to the perovskite structure variations in the band structure and Fermi level in the LSCAOs.

Electronic Structure Analysis. In order to gain a direct and in-depth investigation of the oxidation state variation for the LSCAOs sample. X-ray photoelectron spectroscopy (XPS) results show that the Co 2*p* peak of these samples slightly shift to higher binding energy with the increase of Al concentration (*SI Appendix*, Fig. S10), indicating an increasing in the Co valence state, which is further supported by X-ray absorption near-edge (XANES). The nominal Co valence states are indicated by the K-edge positions when compared to references CoO and Co_3O_4 (*SI Appendix*, Fig. S11; for details, see *SI Appendix*). Although Co^{3+} is more electronegative than Al^{3+}, after Al substitution, the K-edge energies of Co slightly shift to a higher absorption energy compared to LSCO, which indicates an increasing in Co valence state and agrees well with the EELS and XPS result. The valence states of Co atoms of all LSCAOs samples were investigated by XAS to quantitatively characterize the concentration of oxygen defects (*SI Appendix*, Table S2 for details) (28, 29). It can be seen that the concentration of oxygen defects has a negative correlation with the content of Al substitution (Fig. 2*C*); this is in obvious contradiction with the fact that the substitution of Al in LSCAOs reduces the enthalpy of oxygen vacancy formation.

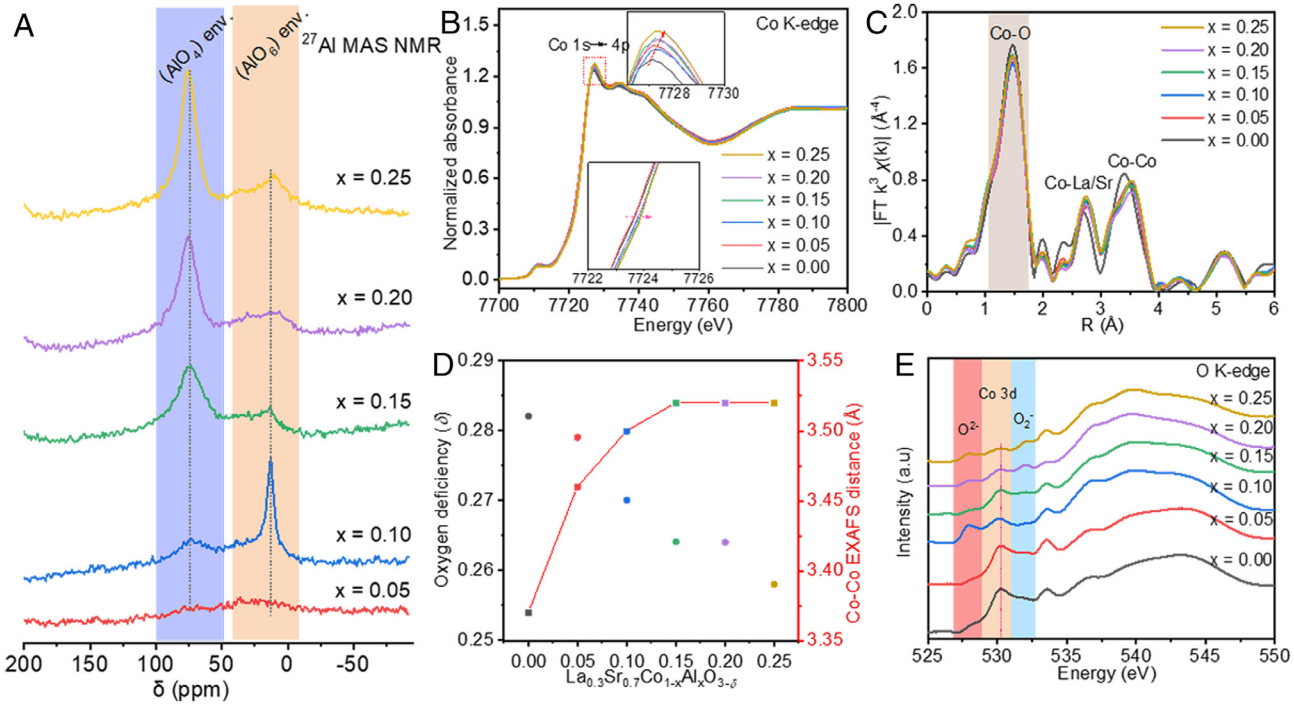

Fig. 2. Environments of Al species and electronic structure characterizations of as-prepared LSCAOs catalysts. (*A*) ^{27}Al MAS NMR spectra recorded at 130.33 MHz using a 30-kHz spinning frequency for LSCAOs with different Al substitution. The signals centered at 0 and 53 ppm were ascribed to octahedrally coordinated (AlO_6 structure unit) and tetracoordinated aluminum (AlO_4 structure unit), respectively. Electronic structure and valence bond information: (*B*) Co K-edge XANES adsorption edges; (*C*) R-space Fourier-transformed FT [$k^4\chi(k)$] of Co K-edge extended X-ray absorption fine structure (EXAFS) for series of LSCAOs. Three dominant peaks were observed at 1.4, 2.7, and 3.3 Å, corresponding Co–O, Co–La/Sr, and Co–Co single scattering, respectively. (*D*) Calculated oxygen deficiencies and Co–Co EXAFS distance of series of LSCAOs. The K-edge position is determined by an integral method as described in *SI Appendix*, Fig. S11 (28, 29), and the details about edge positions and nominal valence state of Co are shown in *SI Appendix*, Table S2. (*E*) The soft X-ray absorption spectra of O K-edges for series of LSCAOs. The peak at about 527 eV is assigned as the pre-edge peak caused by internal charge transfer between Co^{4+} and O^{2-}; the peak at about 530 eV represents the overlapping bands between Co 3*d* and O 2*p*; the peak at about 532 eV is attributed to *s** resonance extinction of O_2^- species; and peaks at about 534 eV and 537 eV are recognized as the hybridization between O 2*p* and La 5*d*/Sr 4*d*/Co 4*sp* in LSCAOs (30–34).

The main reason is due to changes in the local bond. The Co–O bond length bond length increases a bit with the Al substitution ratio from the evidence of extended X-ray absorption fine structure (EXAFS) (Fig. 2 *C* and *D* and *SI Appendix*, Fig. S12). When Al gradually takes the place of the Co atom in LSCAOs, larger Co–O bond length begins to induce lattice distortion in LSCAO, which agrees with FT-IR results. As observed with Co K-edge EXAFS, the first-shell peak at ~1.5 Å, representative of the metal–oxygen bond, and the strength represents the metal–oxygen coordination number (Fig. 2*D* and *SI Appendix*, Fig. S12). Specifically, the EXAFS fitting results (*SI Appendix*, Fig. S13 and Table S3) of the first-shell peak for LSCAOs reveal that Al substitution reduces the average coordination number of Co and O by ~5.4, at maximum. The Co–O EXAFS distance is weakened by Al substitution and appears to be significantly higher for LSCAO x = 0.25. Such an effect indicates a decrease in oxygen vacancies and an increase in cobalt valence state after Al substitution, which is evidenced by the Co K-edge XANES results (*SI Appendix*, Fig. S14). In line with the Fourier transforms, the wavelet transform images reveal a reduced Co–O and extended Co–Co path with the increase of Al doping in as-prepared series of LSCAOs (*SI Appendix*, Fig. S15).

More importantly, the O K-edge XAS is used to determine the essential differences related to Al concentration in the series of LSCAOs (Fig. 2*E*). After Al dopant, the intensity of pre-edge at about 527 eV deservedly increases compared with LSCO and the strongest is reached when x = 0.1, but its peak position remains unchanged, which can be expounded as the increase of concentration for charge transfer between Co^{4+} and O_2^- in LSCAOs. The external electron transfer mode is of promotional significance to activate surface lattice oxygen for obtaining more active O^{2-x} species. Furthermore, the intensity of the Co 3*d*–O 2*p* hybrid peak at about 530 eV is also lower than that of pure LSCO, which be caused by the activation of surface lattice oxygen in LSCAOs ($O^{2-} \rightarrow O^{2-x}$) (30–32). These changes all illustrate that Al dopant reduces electron transfer between Co^{4+} and O_2^- and has a more important effect on optimizing surface electronic state and therefore reduce the overpotential required for OER process on perovskite oxides. Moreover, the synergistic effect narrows the hybridization state between Co 3*d* and O 2*p* and successfully promotes the activation of surface lattice oxygen (33), which can be further evidenced by the O 1*s* energy spectra (*SI Appendix*, Fig. S16 and Table S4). Indeed, the Al substitution in LSCAOs was found to reduce the formation enthalpy of oxygen vacancies, which indicates easier formation of oxygen vacancies, as also supported by theoretical calculations. Introducing constant valence Al into LSCAOs perovskite, the conversion in the valence state of Co (confirmed by XPS and EXAFS analysis) can effectively modulate d electron arrangement and e_g electron number. Magnetism measurement offers a beneficial platform to detect *d* electron arrangement in the LSCAOs sample (34, 35). As observed with magnetic hysteresis loops (*SI Appendix*, Fig. S17), the LSCO is intrinsically nonmagnetic, while the series of LSCAOs exhibit a distinct ferromagnetic feature, which indicates the number of magnetic moments increased after Al of introduction. Subsequently, to further reveal the electron spin configuration of as-prepared series of LSCAOs, we measured the zero-cooled-field and field-cooled temperature-dependent susceptibility curves, as shown in *SI Appendix*, Fig. S18. The effective magnetic moments (μ_{eff}) is directly correlated with the occupancy of the e_g state of CoO_6 octahedra, indicating the higher spin state of LSCAO-0.2 due to strong Jahn–Teller effects with shortening Co–O and elongating Co–Co bonds (*SI Appendix*, Fig. S19 and Table S5) (27, 36, 37), which is consistent with Co K-edge XANES results. Based on the relationship between OER electrocatalytic activity and *d* electron configuration in perovskite-type catalysts, LSCAO-0.2 nanoparticles are expected to be a high-energy OER catalyst (2). All the above results suggest that the reduced Co–O and extended Co–Co bonds contribute to surface reconstruction of the active species.

Electrochemical OER Performance. The perovskite LSCAOs oxide were then measured for their electrocatalytic OER performance under alkaline condition (for details, see *Methods*). Different valance states in different regions of LSCAOs oxide can be validated by experimental cyclic voltammetry (CV) curves, LSCAO-0.2 catalyst exhibits early oxidation peaks of the Co^{2+}/Co^{3+} redox (1.35 V) compared to the LSCO standalone counterpart (*SI Appendix*, Fig. S20). To determine intrinsic activity, specific activities were normalized to the electrocatalytic active surface area (ECSA) of the oxides, which was determined using the double-layer capacitance method to calculate the ECSA of the oxides (*SI Appendix*, Fig. S21). An ohmic drop *iR* correction was applied to compensate potential losses resulting from the resistance of the electrolyte solution (2, 38, 39). As shown in Fig. 3*A*, LSCAO-0.2 is the most effective perovskite oxide. In contrast, as the Al substitution is further increased beyond x = 0.20 in LSCAO, a significant drop in activity is observed. To assess long-term stability, LSCAOs oxide (x = 0, 0.20, and 0.25) was subjected to constant current density of 10 μA cm_{ox}^{-2} in 1 M KOH for 25 h, as illustrated in *SI Appendix*, Fig. S22. Thus, the strong correlation between OER activity and the composition ratio should be ascribed to the perovskite LSCAOs oxide component, which may govern the formation of active sites.

Electrochemical impedance spectroscopy (EIS) was carried out to examine the electrical charge transfer behavior in different phases (40, 41). The results of EIS (*SI Appendix*, Fig. S23) showed that the charge transfer at electrode/electrolyte interfaces in LSCAO-0.2 is more favorable compared to other Al content in LSCAO, as evidenced by the considerable decline in the charge-transfer resistance (R_{ct}). And the charge interaction in the series of LSCAOs is explored by electrical transport measurements (42, 43). The resistivity of the sample was observed to decrease monotonically with increasing Al content (*SI Appendix*, Fig. S24 and Table S6), indicating that it could potentially be a control factor for the amount of Al substitution. As observed in *SI Appendix*, Fig. S25, there is a peak that appears in the Bode phase plot of at different frequency regions. The phase angle of the low-frequency region representing the OER reduced earlier for LSCAO-0.2 (at 1.46 V) compared with LSCO (at 1.51 V) and LSCAO-0.10 (at 1.51 V). Meanwhile, the semicircle of LSCAO-0.2 decreased more rapidly with the increase of potential in the corresponding Nyquist plots, suggesting it was easier to be polarized.

Interpretation of O 2*p*. We have further utilized the density functional theory (DFT) calculation method to investigate the internal driving force, and the projected partial density of states (PDOS) was used to examine changes in the electronic structure. By comparing electronic distributions near the Fermi level (E_F) on the stoichiometric angles of LSCAOs oxide, we observed that both Co 3*d* and La 5*d* orbitals overlap with O 2*p* orbitals, resulting in a stable structure (*SI Appendix*, Fig. S26). The PDOS results indicate that substitution of Al can have varying effects on the O 2*p* and Co 3*d* levels, depending on the level of substitution (as shown in Fig. 3*D*). The *d* band center of LSCAOs oxide shows an obvious N-shape, and Co 3*d* band center of the LSCAO-0.22 shows a sharp peak near the E_F. In addition, the physical origin of the oxidation of lattice oxygen could be attributed to a shift of the E_F deeper into the O 2*p* band in some perovskite oxides

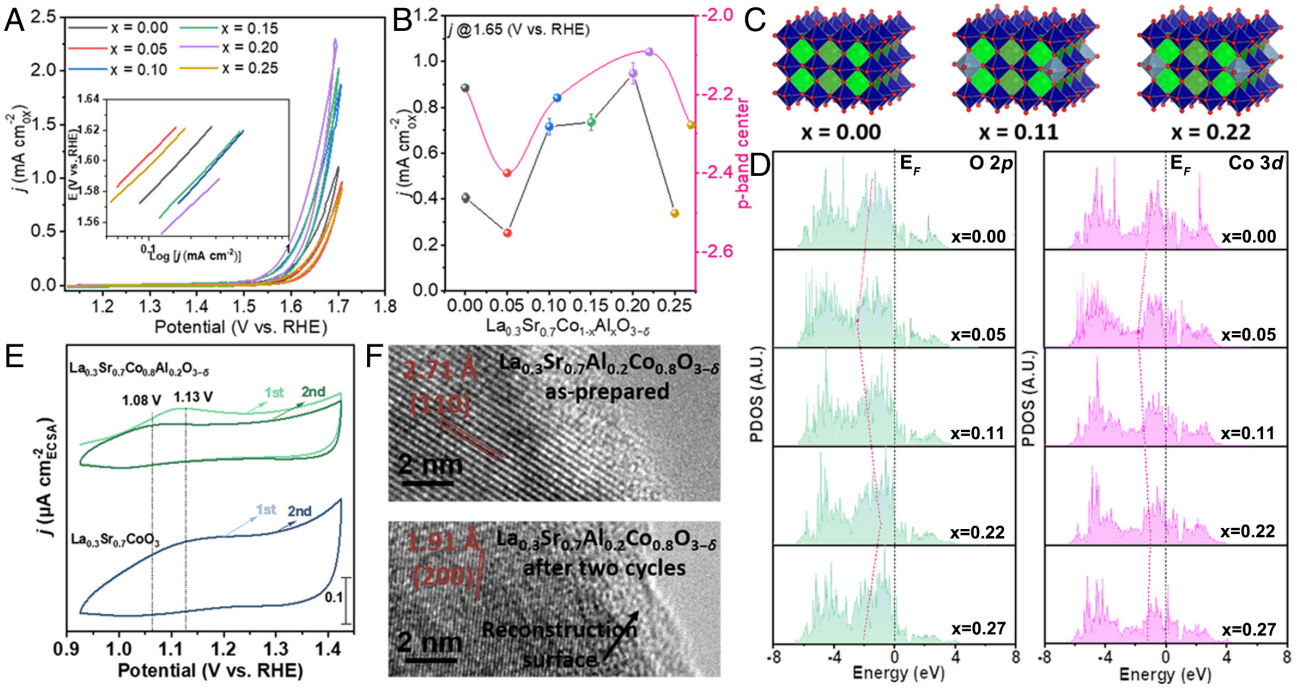

Fig. 3. OER performances of as-prepared LSCAOs catalysts and electronic interpretation of the effect of Al substitution on surface reconstruction. (*A*) CV curves of LSCAOs (x = 0; 0.05; 0.10; 0.15; 0.20; 0.25) in O_2-saturated 1 M KOH with a scan rate of 10 mV s^{-1}. Inset, Corresponding Tafel plots after oxide surface area normalization, capacitance correction, and *i*R correction. (*B*) OER current densities (left axis) of LSCAO at 1.65 V vs. RHE. The O 2*p*−band centre (right axis) in LSCAOs oxide is plotted to show its correlation with OER activity. (*C*) Computational models of LSCAOs (x = 0; 0.11; 0.22). (*D*) The *d*−band center of Co−3*d* and *p*−band center of O 2*p* PDOS in LSCAOs. (*E*) Pseudocapacitive behavior in the first and second cycles of LSCO and LSCAO-0.2 during CV cycling. (*F*) HRTEM images, showing the surface regions for as-prepared LSCAO-0.2 and after two cycles.

(11, 15, 17, 42, 43). The alignment of the O 2*p* band center with respect to the E_F is observed to correspond to the energy of the O_2/H_2O redox potential of the LSCAOs oxide (Fig. 3*B*; for more detail see *SI Appendix*, Table S7). Interestingly, the change of the O 2*p* band center caused by Al substitution is consistent with the change in oxygen vacancy formation energy in LSCAOs perovskite oxide (*SI Appendix*, Table S8). Therefore, due to the upshifted O 2*p* level, it is expected that the oxidation of lattice oxygen in LSCAO-0.22 will be more favorable compared to that in LSCO and LSCAO-0.11 (44, 45). It is noted that the *p*-band center and *d*-band center show a consistent trend, which means that the metal–oxygen hybridization is not weakened to improve the OER performances. The substitution of oxides has a similar effect on the structural analysis, where the inclusion of Al continuously increases, the external electron transfer mode is of promotional significance to activate surface lattice oxygen for obtaining more active O^{2-x} species. This results in the accumulation of oxygen vacancy on the oxide surface, leading to the reconstitution of the surface as hydroxide under alkaline conditions when lattice-oxygen oxidation occurs (46).

Surface Reconstruction in OER. Monitoring the dynamic changes behavior at metal sites provides an opportunity to identify the source of activity during the electrochemical process (47–49). It is important to note that there is minimal change in the valence of La, Sr, and Al in LSCAO-0.2, but the local atomic structure of Co sites in LSCO-0.2 changes during the OER, as shown in *SI Appendix*, Fig. S27. In order to investigate the preoxidation of Co(iii) in LSCO, LSCAO-0.1, and LSCAO-0.2, their CVs (first and second cycles) were examined. For LSCAO-0.2, the first cycle displays a larger pseudocapacitive charge than the second cycle, and the CV profiles of LSCO and LSCAO-0.1 exhibit negligible changes (Fig. 3*E* and *SI Appendix*, Fig. S28*A*). This electrochemical behavior indicates that the surface reconfiguration on the catalyst surface is most likely caused by four-coordinate Al surface reconstruction into the oxyhydroxide, resulting in a stable OER catalytic surface. Our findings indicate that the formation of oxyhydroxide demonstrates varying pseudocapacitive behaviors depending on the coordination environment of the Al. To be specific, the anodic peak in the first cycle appears at ~1.12 V for LSCAO-0.2, whereas a much more anodic peak is observed for LSCO (~1.14 V) and LSCAO-0.1 (~1.15 V), suggesting that four-coordinate Al promotes the preoxidation of Co(ii) and facilitates the subsequent formation of Co oxyhydroxide. Significant differences in oxidation peaks and pseudocapacitive charges are observed between the first and second cycles for LSCAO-0.2, indicating a change in surface chemistry, while no such contrast is observed for LSCO and LSCAO-0.1. Further reconstruction is expected to occur on the surface of LSCAO-0.2, as supported by the results of scanning transmission electron microscopy coupled with high-resolution TEM (HRTEM) shown in Fig. 3*F* and *SI Appendix*, Fig. S28. The reconstructed surface of the resulting hydroxide oxide can be observed under HRTEM, indicating a change in surface chemistry from oxide to hydroxide due to reconfiguration.

Based on the results, we propose two proton/electron transfer processes for evolving active oxygen sites on the LSCAO-0.2 surface. As also observed in pH-dependence measurements, LSCAO-0.1 and LSCAO-0.2 show significant pH-dependent OER activity as observed in Fig. 4*A*, whereas the LSCO does not. This effect is driven by a pH-sensitive surface reconstruction, which indicates a possible decoupling of the proton/electron transfer process, such as lattice-oxygen oxidation (3, 11, 12, 50). Such decoupled proton/electron transfer process is also evidenced by coupled with ^{18}O isotope-labeling differential electrochemical mass spectrometry (DEMS; Fig. 4 *B*–*D*) (11, 51). The degree of lattice-oxygen

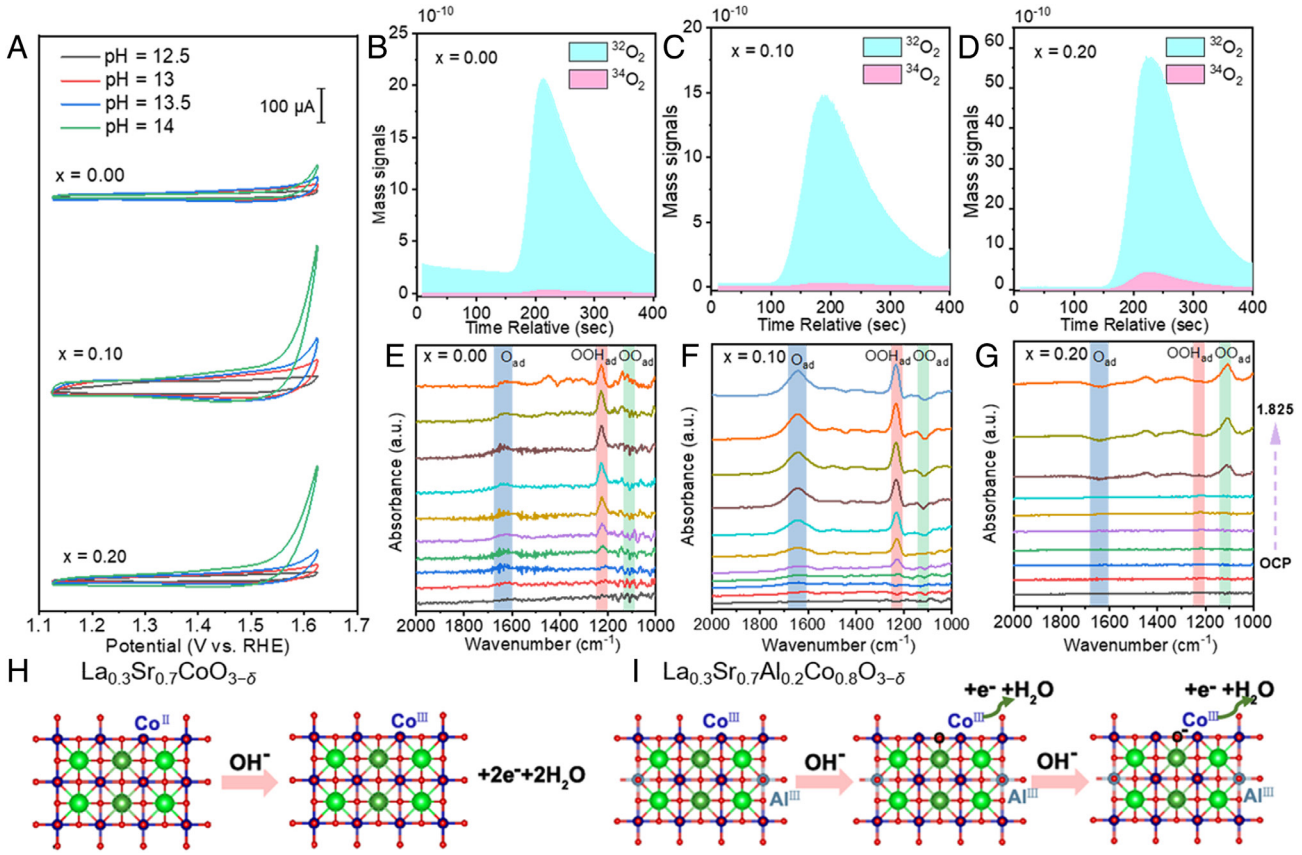

Fig. 4. In situ investigation of pre-OER behaviors of catalysts and schematic of the surface reconstruction and deprotonation process. (*A*) CVs of LSCAO (x = 0.0, 0.10 and 2.0) scanned in O_2-saturated KOH (pH ≈ 12.5 to 14) at a scan rate of 10 mV s^{-1}. DEMS signal ratios of $^{34}O_2$ ($^{16}O^{18}O$) and $^{32}O_2$ ($^{16}O^{16}O$) from the reaction products for ^{18}O-labeled. (*B*) LSCO, (*C*) LSCAO-0.1, and (*D*) LSCAO-0.2 catalyst tests in $H_2{}^{16}O$ aqueous KOH electrolyte. In situ ATR-IR spectra recorded during the multi-potential steps for (*E*) LSCO (*F*) LSCAO-0.1 and (*G*) LSCAO-0.2. Proposed deprotonation mechanism before OER, shown for (*H*) LSCO and (*I*) LSCAO-0.2. The absorption band peaked at around 1,212 cm^{-1} is ascribed to the O–O stretching mode of surface-adsorbed superoxide (OOH_{ad}), the band at around 1,400 and 1,650 cm^{-1} are attributed to the O–O stretching mode of weakly adsorbed molecular oxygen (52, 53).

oxidation participation at LSCAO-0.2 is increased by 4.8 times that of LSCO. To investigate the mechanism for the generation of O_2, in situ attenuated total reflection infrared spectra (ATR-IR; Fig. 4 *E* and *F* and *SI Appendix*, Fig. S29) were performed to capture the adsorbed intermediate (40, 52, 53). It is noteworthy that OOH_{ad} species and O_{ad} species appeared at the OCV for LSCO and LSCAO-0.1, while it did not emerge until 1.825 V for LSCAO-0.2, and the bands at around 1,400 and 1,650 cm^{-1} appeared at 1.625 V for LSCAO-0.2 while it emerged at 1.825 V for LSCO, suggests that the lattice-oxygen oxidation dominates the O_2 generation of LSCAO-0.2. These further indicate that four-coordinate Al may promote deprotonation process through two proton/electron transfer processes, resulting in the evolution of active oxygen sites. The Al doping is also beneficial to the formation of active phase and the improvement of catalytic activity of materials.

Reconstruction Terminating with Al^{3+} Leaching. The study suggests that active oxyhydroxides produce reactive oxygen species during the anodic scanning step, which serves as the final active site. Quasi in situ XANES analysis was conducted to examine the dynamic valence state of Co on LSCAO-0.2 during OER. Fig. 5*A* displays the Co K-edge XANES of LSCAO-0.2 oxides recorded at 1.175 to 1.625 V (vs. RHE). The XANES results show that the Co K-edges of both oxides have shifted to lower energy. This is because more O^{2-x} species appear during the OER process, which represents that there is electron transfer from O sites to nearby Co sites. Then, this will lead to a decrease in Co valence states. In the pseudocapacitive region (Fig. 5*B* and *SI Appendix*, Fig. S30), the Co–O and Co–Co EXAFS distance increment is primarily observed in regions I (1.05 to 1.40 V) and II (1.40 to 1.52 V), while the Co behavior in the pre-OER stage can be found in region III (1.52 to 1.625 V). The increase in Co valency can be attributed to a deprotonation process on the reconstructed surface of the catalysts. Therefore, the reason for the enhanced OER activity is that four-coordinate Al promotes the deprotonation process, leading to the formation of an active oxygen surface at a low potential.

Importantly, the original main crystal structure of the catalyst remained unchanged after catalysis, as shown in the XRD (*SI Appendix*, Fig. S31) and HAADF-STEM images (*SI Appendix*, Fig. S32). However, the XRD pattern does not obviously change after catalysis, and a small impurity peak appears with the increase of Al. To understand the mechanism of surface reconstruction, XPS spectra were collected after durability tests. The binding energy of Co 2*p* in all samples shifted positively due to the transformation from oxide to oxyhydroxide (*SI Appendix*, Fig. S33). The prominent peak at ~529 eV is attributed to the M–O bond, which decreased noticeably after OER. This provides additional evidence for the formation of an oxyhydroxide phase during the catalytic process. Notably, LSCAO-0.2 exhibits stable surface chemistry and becomes significantly amorphous after reconstruction. It was found that the reconstruction caused by lattice-oxygen oxidation stops after the first cycle, and the reconstructed surface remains highly active and stable in subsequent cycles. In order to investigate the mechanism of this reconstruction termination, we quantitatively determined the leached amounts of cations on the electrolyte during OER using

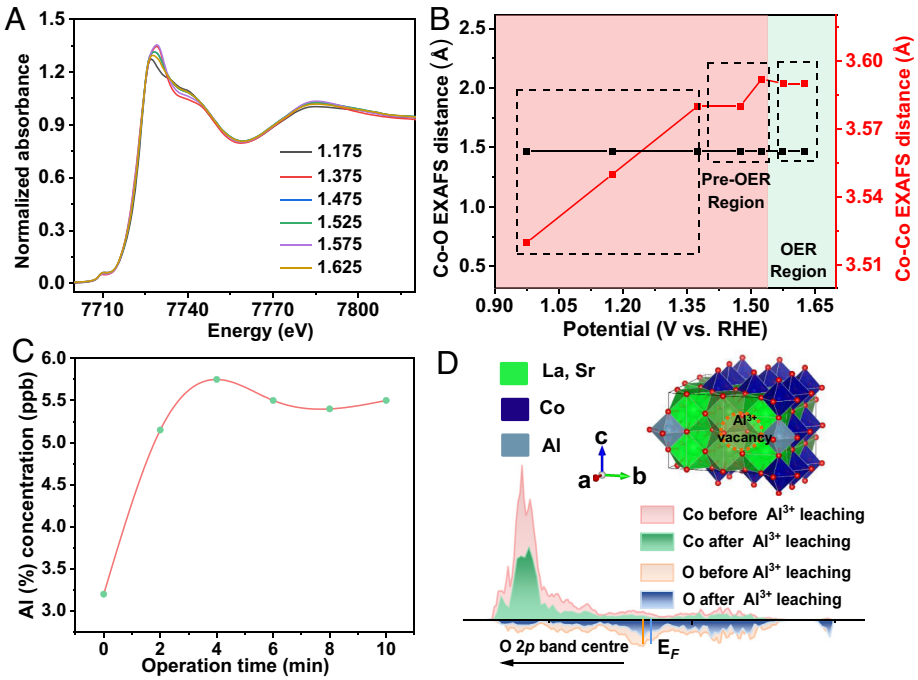

Fig. 5. Reconstruction terminating mechanism with Al^{3+} leaching. (*A*) Normalized ex-situ Co K-edge XANES analysis of LSCAO-0.2 under 1.175, 1.375, 1.475, 1.575, and 1.625 V (vs. RHE), as well as the FT $k^4\chi(R)$ Co K-edge EXAFS. (*B*) Calculated Co−O and Co−Co EXAFS distance of LSCAO-0.2 under different potentials. (*C*) ICP-MS test of the electrolyte for LSCAO-0.2 under an operation time of 0 to 10 min (in 1 M KOH under 20 μA cm_{ox}^{-2}). The dissolubility of Al in terms of $Al(OH)_4^-$ is far beyond the concentration of Al^{3+} in our tested electrolytes. (*D*) Computational model for LSCAO-0.22 after Al^{3+} leaching and schematic band diagrams of LSCAO-0.22 with and without Al^{3+} vacancies. The perovskite structure beneath the reconstructed surface was confirmed by the atomic-resolution HAADF-STEM image (*SI Appendix*, Fig. S32).

inductively coupled plasma mass spectrometry. An operando timeline revealed that leaching of Al cations dissolutions finished quickly as the OER proceeded, and no notable Al leaching was observed thereafter for the LSCAO-0.2. Additionally, leaching of Co cations was almost negligible (Fig. 5*C*). The leaching of Al is believed to be connected to the reconstruction process. The results indicate that the initial Al leaching is accompanied by reconfiguration, which alters the local electronic structure of the oxides and prevents further reconfiguration. Furthermore, the local electronic structure of the lattice with Al^{3+} leaches was studied using DFT calculations (Fig. 5*D* and *SI Appendix*, Fig. S34). The introduction of Al^{3+} leaches into the lattice causes a decrease in energy at the O 2*p* level. This decrease in energy terminates lattice-oxygen oxidation and surface reconstruction, as there are no more oxygen vacancies produced. This leads to a more stable surface chemistry.

Conclusions

Using OER as a model reaction, we show that Al substitution aids in the surface reconstruction of LSCAOs. Through precise synthesis, we were able to quantitatively introduce Al into the material and identify two types of aluminum environments: AlO_6 octahedra and AlO_4 tetrahedra. Significantly, we found that the AlO_4 tetrahedra activate two deprotonation processes in reconstructed oxyhydroxides, resulting in the formation of active oxygen species at a low overpotential. DFT calculations show that Al substitution leads to an increase in the O 2*p* level, which promotes the generation of surface oxygen vacancies and lattice-oxygen oxidation under OER conditions. This substitution also provides greater structural flexibility for reconstruction. However, as Al^{3+} leaches during the initial stages of reconstruction, the O 2*p* level decreases in energy, ultimately resulting in a stable surface chemistry due to the termination of surface reconstruction. The study shows that LSCAO-0.2 has exceptional intrinsic activity, mass efficiency, and stability when used for the OER. The research provides a valuable approach to enhance the coordination between the catalysts' activity and stability by adjusting the dynamic reconstruction during an electrocatalysis process, which leads to the formation of active sites.

Materials and Methods

Materials. $La(NO_3)_3\,6H_2O$, $Sr(NO_3)_2\,6H_2O$, $Co(NO_3)_2\,6H_2O$, $Al(NO_3)_3{\cdot}6H_2O$, polyvinyl alcohol (PVA), citric acid, and KOH (99%) were purchased from Innochem; Nafion® perfluorinated resin solution in lower aliphatic alcohols and water (5 wt%) was purchased from Sigma-Aldrich, and absolute ethanol and isopropanol were purchased from Aladdin. The demonized (DI) water was obtained from a Millipore Auto-pure system (18.2 M, Millipore Ltd., (USA). All the other materials for electrochemical measurements were of analytical grade without further purification.

Synthesis of Bulk $La_{0.3}Sr_{0.7}Co_{1-x}Al_xO_{3-\delta}$. LSCAOs bulk powder was synthesized using sol–gel methods using stoichiometric amounts (according to the molecular formula) of $La(NO_3)_3\,6H_2O$, $Sr(NO_3)_2\,6H_2O$, $Co(NO_3)_2\,6H_2O$, and $Al(NO_3)_3\,6H_2O$. The above metal nitrates were dissolved in appropriate DI water under stirring until completely dissolved, and then, 10 mL 2 wt% PVA and citric acid (3 times the total molar amount of metal ions) were added to the solution under stirring, followed by adjusting the pH of the solution to 8 by addition of aqueous NH_4OH. The transparent solution was vigorously stirred at room temperature for 2 h. They were further continually stirred at 120 °C until transparent and viscous gel formed. The resulting gel was dried for 10 h at 200 °C, and the obtained black gray precursor was crushed and calcined at 750 °C for 5 h and 950 °C for 8 h with a heating speed of 2 °C min^{-1} and then cooled down to room temperature naturally.

DEMS Measurements. DEMS measurements were carried out to determine the ^{18}O-labeled OER reaction products of LSCO, LSCAO-0.1, and LSCAO-0.2 catalysts during the OER process using a QAS 100 device (Linglu Instruments, Shanghai). A saturated Ag/AgCl electrode and a Pt wire were used as the reference electrode and counter electrode, respectively. The working electrodes were prepared by sputtering Au onto 50-μm-thick porous polytetrafluoroethylene films. Then, the

catalysts were drop-cast onto the Au with a loading mass of 1 mg cm^{-2}. First, the catalysts were labeled with ^{18}O isotopes by performing 10 CV cycles at a scan rate of 10 mV/s in ^{18}O-labeled 1 M KOH solution between 0.2 and 0.8 V Ag/AgCl. Afterward, ^{18}O-labeled electrodes were rinsed five times with ^{16}O water to remove the remaining $H_2{}^{18}O$. Last, the electrodes were subjected to CV cycles in ^{16}O 1 M KOH solution at the above potential window and scan rate. In the meantime, gas products of different molecular weights generated during the OER process were measured in real time by mass spectroscopy. Since catalysts were thoroughly rinsed with ^{16}O water after ^{18}O labeling, it is unlikely that ^{18}O species adsorbed on the surface contribute substantially to the observed $^{34}O_2$ ($^{16}O^{18}O$) signals. Thus, the participation of lattice oxygen from catalysts in OER can be determined by measuring the $^{34}O_2$ signals.

In Situ ATR-IR Spectra. ATR-IR spectra were investigated using a customized cell, with a saturated Ag/AgCl reference electrode and a Pt ring counter electrode in 1 M KOH. In situ electrochemical characterization was carried out at a specific potential for 10 min to obtain the surface chemical composition and structural information of materials.

Computational Details. All the calculations are performed in the framework of the DFT with the projector augmented plane-wave method, as implemented in the Vienna ab initio simulation package (54). The nuclei–electron and the electron exchange correlation interactions were described by the projector augmented wave potentials (55) and the generalized gradient approximation (56) with the Perdew–Burke–Ernzerhof (57) functional, respective. The DFT models are built based on the TEM and ^{27}Al MAS NMR spectra results of experiments. Regarding the LSCO model, the bulk lattice was built based on the relaxed cubic LCO_t of which the bandgap width was 1.513 eV for LCO and a = b = c = 3.828 Å. The $La_{0.6}Sr_{1.4}Co_{2-2x}Al_{2x}O_6$ was built with 70% of La sites that were replaced by Sr sites and x% of Co sites that were replaced by Al sites, of which the minimum unit cell parameters were a = b = 3.821 Å and c = 7.656 Å. The supercell model was built with 100 atoms. The cut-off energy for plane wave is set to 500 eV. The energy criterion is set to 10^{-4} eV in iterative solution of the Kohn–Sham equation. The Brillouin zone integration is performed using a 3 × 3 × 4 k-mesh. All the structures are relaxed until the residual forces on the atoms have declined to less than 0.05 eV/Å.

The oxygen vacancy formation energies (ΔG) were obtained by (58)

$$E_f = E\left(V_0\right) - E\left(\text{bulk}\right) + \mu_0,$$

where $E(V_0)$ is the total energy derived from a supercell calculation with one O vacancy in the cell, and E(bulk) is the total energy for the equivalent supercell containing only bulk materials. μ_0 is the corresponding chemical potentials of O, and μ_0 is defined as (59)

$$\mu_0 = 1/2E_{02} + 1/2kT\ln\left(pV_Q/kT\right),$$

where V_Q is quantum volume, and E_{02} is the energy of O_2 in 0 K.

Data, Materials, and Software Availability. All study data are included in the article and/or *SI Appendix*.

ACKNOWLEDGMENTS. We acknowledge support from the National Key R&D Program of China (2021YFA1501101), the National Natural Science Foundation of China (No. 22221001, 22271124, and 21931001), Special Fund Project of Guiding Scientific and Technological Innovation Development of Gansu Province (2019ZX-04), the 111 Project (B20027), and the Fundamental Research Funds for the Central Universities (lzujbky-2023-eyt03). We also appreciate Si-Min Yu from the Lanzhou Magnetic Resonance Center for her help with solid-state NMR characterization.

Author affiliations: [a]State Key Laboratory of Applied Organic Chemistry, Frontiers Science Center for Rare Isotopes, College of Chemistry and Chemical Engineering, Lanzhou University, Lanzhou 730000, China; [b]State Key Laboratory of Baiyunobo Rare Earth Resource Researches and Comprehensive Utilization, Baotou Research Institute of Rare Earths, Baotou 014030, China; and [c]Beijing National Laboratory for Molecular Sciences, State Key Laboratory of Rare Earth Materials Chemistry and Applications, Peking University-The University of Hong Kong Joint Laboratory in Rare Earth Materials and Bioinorganic Chemistry, College of Chemistry and Molecular Engineering, Peking University, Beijing 100871, China

1. J. Hwang *et al.*, Perovskites in catalysis and electrocatalysis. *Science* **358**, 751–756 (2017).
2. W. T. Hong *et al.*, Toward the rational design of non-precious transition metal oxides for oxygen electrocatalysis. *Energy Environ. Sci.* **8**, 1404–1427 (2015).
3. T. Wu *et al.*, Iron-facilitated dynamic active-site generation on spinel $CoAl_2O_4$ with self-termination of surface reconstruction for water oxidation. *Nat. Catal.* **2**, 763–772 (2019).
4. O. Hansen, B. Seger, P. C. K. Vesborg, I. Chorkendorff, A quick look at how photoelectrodes work. *Science* **350**, 1030–1031 (2015).
5. I. E. Castelli *et al.*, New cubic perovskites for one- and two-photon water splitting using the computational materials repository. *Energy Environ. Sci.* **5**, 9034–9043 (2012).
6. J.-I. Jung *et al.*, Optimizing nanoparticle perovskite for bifunctional oxygen electrocatalysis. *Energy Environ. Sci.* **9**, 176–183 (2016).
7. E. McCalla *et al.*, Visualization of O–O peroxo-like dimers in high-capacity layered oxides for li-ion batteries. *Science* **350**, 1516–1521 (2015).
8. M. Sathiya *et al.*, Reversible anionic redox chemistry in high-capacity layered-oxide electrodes. *Nat. Mater.* **12**, 827–835 (2013).
9. W. Huang *et al.*, Isolated electron trap-induced charge accumulation for efficient photocatalytic hydrogen production. *Angew. Chem. Int. Ed.* **62**, e202304634 (2023).
10. H. Zhang, X. W. Lou, 3D printing of single-atom catalysts. *Nat. Synth.* **2**, 81–82 (2023).
11. A. Grimaud *et al.*, Activating lattice oxygen redox reactions in metal oxides to catalyse oxygen evolution. *Nat. Chem.* **9**, 457–465 (2017).
12. M. T. M. Koper, Theory of multiple proton-electron transfer reactions and its implications for electrocatalysis. *Chem. Sci.* **4**, 2710–2723 (2013).
13. I. C. Man *et al.*, Universality in oxygen evolution electrocatalysis on oxide surfaces. *Chem. Catal. Chem.* **3**, 1159–1165 (2011).
14. L. An *et al.*, Recent development of oxygen evolution electrocatalysts in acidic environment. *Adv. Mater.* **33**, 2006328 (2021).
15. A. Grimaud *et al.*, Double perovskites as a family of highly active catalysts for oxygen evolution in alkaline solution. *Nat. Commun.* **4**, 2439 (2013).
16. Y. Zhu *et al.*, Boosting oxygen evolution reaction by creating both metal ion and lattice-oxygen active sites in a complex oxide. *Adv. Mater.* **32**, 1905025 (2020).
17. Y.-L. Lee, J. Kleis, J. Rossmeisl, Y. Shao-Horn, D. Morgan, Prediction of solid oxide fuel cell cathode activity with first-principles descriptors. *Energ. Environ. Sci.* **4**, 3966–3970 (2011).
18. J. K. Nørskov, T. Bligaard, J. Rossmeisl, C. H. Christensen, Towards the computational design of solid catalysts. *Nat. Chem.* **1**, 37–46 (2009).
19. F. Fang *et al.*, Construction of a hollow structure in $La_{0.9}K_{0.1}CoO_{3-\delta}$ nanofibers via grain size control by Sr substitution with an enhanced catalytic performance for soot removal. *Catal. Sci. Technol.* **9**, 4938–4951 (2019).
20. M. Zayat, D. Levy, Blue $CoAl_2O_4$ particles prepared by the sol-gel and citrate-gel methods. *Chem. Mater.* **12**, 2763–2769 (2000).
21. M. E. Smith, Application of ^{27}Al NMR Techniques to Structure Determination in Solids. *Appl. Magn. Reson.* **4**, 1–64 (1993).
22. L. A. O'Dell, S. L. P. Savin, A. V. Chadwick, M. E. Smith, A ^{27}Al MAS NMR study of a sol-gel produced alumina: Identification of the NMR parameters of the θ-Al_2O_3 transition alumina phase. *Solid State Nucl. Magn. Reson.* **31**, 169–173 (2007).
23. L. Samain *et al.*, Structural analysis of highly porous γ-Al_2O_3. *J. Solid State Chem.* **217**, 1–8 (2014).
24. C. Tealdi *et al.*, Average versus local structure in K_2NiF_4-type $LaSrAlO_4$: Direct experimental evidence of local cationic ordering. *J. Mater. Chem.* **22**, 10488–10495 (2012).
25. N. Pellerin, C. Dodane-Thiriet, V. Montouillout, M. Beauvy, D. Massiot, Cation sublattice disorder induced by swift heavy ions in $MgAl_2O_4$ and $ZnAl_2O_4$ Spinels: ^{27}Al solid-state NMR study. *J. Phys. Chem. B* **111**, 12707–12714 (2007).
26. H. Liang *et al.*, Influence of partial Mn-substitution on surface oxygen species of $LaCoO_3$ catalysts. *Catal. Today* **201**, 98–102 (2013).
27. Y. Duan *et al.*, Tailoring the Co 3*d*–O 2*p* covalency in $LaCoO_3$ by Fe substitution to promote oxygen evolution reaction. *Chem. Mater.* **29**, 10534–10541 (2017).
28. H. Dau, P. Liebisch, M. Haumann, X-ray absorption spectroscopy to analyze nuclear geometry and electronic structure of biological metal centers—Potential and questions examined with special focus on the tetra-nuclear manganese complex of oxygenic photosynthesis. *Anal. Bioanal. Chem.* **376**, 562–583 (2003).
29. M. Lu *et al.*, Artificially steering electrocatalytic oxygen evolution reaction mechanism by regulating oxygen defect contents in perovskites. *Sci. Adv.* **8**, eabq3563 (2022).
30. X. Li *et al.*, Au/3DOM $LaCoO_3$: High-performance catalysts for the oxidation of carbon monoxide and toluene. *Chem. Eng. J.* **228**, 965–975 (2013).
31. L. Karvonen *et al.*, O-K and Co-L XANES study on oxygen intercalation in perovskite $SrCoO_{3-\delta}$. *Chem. Mater.* **22**, 70–76 (2010).
32. X. Wang *et al.*, Activation of surface oxygen sites in a cobalt-based perovskite model catalyst for CO oxidation. *J. Phys. Chem. Lett.* **9**, 4146–4154 (2018).
33. F. Frati, M. O. Hunault, F. M. De Groot, Oxygen K-edge X-ray absorption spectra. *Chem. Rev.* **120**, 4056–4110 (2020).
34. S. Zhou *et al.*, Engineering electrocatalytic activity in nanosized perovskite cobaltite through surface spin-state transition. *Nat. Commun.* **7**, 11510 (2016).
35. A. Vojvodic, J. K. Nørskov, Optimizing perovskites for the water-splitting reaction. *Science* **334**, 1355–1356 (2011).
36. Y. Tong *et al.*, Vibronic superexchange in double perovskite electrocatalyst for efficient electrocatalytic oxygen evolution. *J. Am. Chem. Soc.* **140**, 11165–11169 (2018).
37. M. A. Halcrow, Jahn-teller distortions in transition metal compounds, and their importance in functional molecular and inorganic materials. *Chem. Soc. Rev.* **42**, 1784–1795 (2013).
38. J. Yin *et al.*, Iridium single atoms coupling with oxygen vacancies boosts oxygen evolution reaction in acid media. *J. Am. Chem. Soc.* **142**, 18378–18386 (2020).
39. J. Yin *et al.*, Oxygen vacancies dominated NiS_2/CoS_2 interface porous nanowires for portable Zn–air batteries driven water splitting devices. *Adv. Mater.* **29**, 1704681 (2017).
40. L. An *et al.*, Epitaxial heterogeneous interfaces on N-$NiMoO_4/NiS_2$ nanowires/nanosheets to boost hydrogen and oxygen production for overall water splitting. *Adv. Funct. Mater.* **29**, 1805298 (2019).

41. N. Zhang *et al.*, Surface activation and Ni–S stabilization in NiO/NiS_2 for efficient oxygen evolution reaction. *Angew. Chem. Int. Ed.* **61**, e202207217 (2022).
42. J. T. Mefford *et al.*, Water electrolysis on $La_{1-x}Sr_xCoO_{3-\delta}$ perovskite electrocatalysts. *Nat. Commun.* **7**, 11053 (2016).
43. X. Cheng *et al.*, Oxygen evolution reaction on La1–xSrxCoO3 perovskites: A combined experimental and theoretical study of their structural, electronic and electrochemical properties. *Chem. Mater.* **27**, 7662–7672 (2015).
44. J. B. Goodenough, Perspective on engineering transition-metal oxides. *Chem. Mater.* **26**, 820–829 (2013).
45. K. J. May *et al.*, Influence of oxygen evolution during water oxidation on the surface of perovskite oxide catalysts. *J. Phys. Chem. Lett.* **3**, 3264–3270 (2012).
46. M. M. Koper, Volcano activity relationships for proton-coupled electron transfer reactions in electrocatalysis. *Top. Catal.* **58**, 1153–1158 (2015).
47. S. Zuo, Z. P. Wu, H. Zhang, X. W. Lou, Operando monitoring and deciphering the structural evolution in oxygen evolution electrocatalysis. *Adv. Energy Mater.* **12**, 2103383 (2022).
48. J. G. McAlpin *et al.*, EPR evidence for Co(iv) species produced during water oxidation at neutral pH. *J. Am. Chem. Soc.* **132**, 6882–6883 (2010).
49. A. Grimaud *et al.*, Activation of surface oxygen sites on an iridium-based model catalyst for the oxygen evolution reaction. *Nat. Energy* **2**, 16189 (2017).
50. L. Giordano *et al.*, pH dependence of OER activity of oxides: Current and future perspectives. *Catal. Today* **262**, 2–10 (2016).
51. P. Zhang *et al.*, Dendritic core-shell nickel–iron–copper metal/metal oxide electrode for efficient electrocatalytic water oxidation. *Nat. Commun.* **9**, 381 (2018).
52. Y. Yao *et al.*, Engineering the electronic structure of single atom Ru sites via compressive strain boosts acidic water oxidation electrocatalysis. *Nat. Catal.* **2**, 304–313 (2019).
53. S. Nayak, I. J. McPherson, K. A. Vincent, Adsorbed intermediates in oxygen reduction on platinum nanoparticles observed by in situ IR spectroscopy. *Angew. Chem. Int. Ed.* **57**, 12855–12858 (2018).
54. G. Kresse, D. Joubert, From ultrasoft pseudopotentials to the projector augmented-wave method. *Phys. Rev. B* **59**, 1758–177 (1999).
55. P. E. Blöchl, Projector augmented-wave method. *Phys. Rev. B* **50**, 17953–17979 (1994).
56. J. P. Perdew, K. Burke, M. Ernzerhof, Generalized gradient approximation made simple. *Phys. Rev. Lett.* **77**, 3865–3868 (1996).
57. J. P. Perdew, M. Ernzerhof, K. Burke, Rationale for mixing exact exchange with density functional approximations. *J. Chem. Phys.* **105**, 9982–9985 (1996).
58. C. G. Van de Walle, J. Neugebauer, First-principles calculations for defects and impurities: Applications to III-nitrides. *J. Appl. Phys.* **95**, 3851–3879 (2004).
59. H. Iddir, S. Öğüt, P. Zapol, N. D. Browning, Diffusion mechanisms of native point defects in rutile TiO_2: Ab initio total-energy calculations. *Phys. Rev. B* **75**, 073203 (2007).